RSC Advances

PAPER

View Article Online
View Journal | View Issue

Open Access Article. Published on 15 July 2024. Downloaded on 11/10/2025 11:29:51 AM.
This article is licensed under a Creative Commons Attribution-NonCommercial 3.0 Unported Licence.

Check for updates

Cite this: *RSC Adv.*, 2024, **14**, 22420

Preparation and performance study of *in situ* mineralized bone tissue engineering scaffolds

Chunyan Tian,[a] Kun Li,[a] Fuhuan Chu,[a] Qiujiang Wei,[a] Shiqi Xu,[*abc] Linhui Qiang[*abc] and Xinrui Gou[a]

Traditional bone tissue engineering techniques require the extraction and proliferation of seed cells, followed by prolonged *in vitro* culture to form bone tissue constructs. In contrast, *in situ* mineralization bone tissue engineering utilizes alkaline phosphatase within the body's microenvironment to induce scaffold mineralization. This approach promotes further proliferation and differentiation of osteoblasts and the formation of bone tissue constructs, thereby simplifying the traditional bone tissue engineering process. This study uses electrospinning technology to prepare a novel biologically active scaffold for bone tissue engineering using poly(lactic-*co*-glycolic acid) (PLGA) and calcium glycerophosphate. The morphology and composition of the scaffolds were characterized using SEM, EDS, and XRD, revealing well-defined fibrous structures and the successful incorporation of calcium glycerophosphate into the PLGA fibers. *In vitro* simulation of the bone microenvironment using alkaline phosphatase effectively catalyzed the *in situ* mineralization of calcium glycerophosphate within the scaffold. SEM observations showed substantial mineral aggregation on the surface of the fibrous membranes, and XRD characterization confirmed that the diffraction peaks of the minerals correspond to hydroxyapatite. The cytotoxicity, cell proliferation, and osteogenic differentiation assessments on MC3T3-E1 pre-osteoblasts cultured on the prepared scaffolds indicate that the scaffolds are non-toxic to cells and possess good osteogenic differentiation ability, enabling *in situ* mineralization. This suggests that the scaffolds have broad prospects for application in bone defect repair.

Received 3rd June 2024
Accepted 8th July 2024

DOI: 10.1039/d4ra04047c

rsc.li/rsc-advances

1 Introduction

The skeletal system is crucial in supporting and protecting the human body.[1] Accidents, diseases, tumors, and other causes can all lead to bone defects, and treating this problem still presents significant challenges. Bones can regenerate and repair themselves to a certain extent. Still, large areas of bone defects cannot heal on their own,[2,3] and require external intervention and assistance to promote bone regeneration in the affected area.[4] Clinical methods used for bone tissue regeneration include autografts, allografts, demineralized allografts, and artificial bone substitutes.[5] Autografts are currently considered the gold standard for treating bone defect diseases.[5–7] But autologous bone transplantation is derived from the patients themselves, and the source is limited. Xenograft bone transplantation can reduce unnecessary trauma for patients and does not carry the risks of immune rejection or disease transmission. However, xenograft materials, such as deproteinized bovine bone matrix, often lack osteoinductive and osteogenic properties.[8]

In recent years, tissue engineering has provided a new approach to treating bone defects.[9–11] Tissue engineering approaches involve pre-fabricating scaffolds, which are then seeded with cells and growth factors. After a period of *in vitro* cultivation, these constructs are transplanted *in vivo* to accelerate bone regeneration at defect sites.[12–14]

The preparation of tissue engineering scaffolds mainly involves technologies such as electrospinning, 3D printing, and the sol–gel method. Electrospinning is a commonly employed method for fabricating nanofibrous scaffolds for tissue engineering. This technique utilizes electrostatic forces to draw polymer solutions into fibers, which are subsequently collected to form the desired fibrous membrane scaffolds.[15,16] This technique offers the advantage of controlling fiber diameter, morphology, and surface characteristics, resulting in fibrous scaffolds with excellent porosity and structural features. These properties facilitate cell adhesion, proliferation, and tissue regeneration.[17,18]

In tissue engineering for bone defect repair, cells need to be cultured *in vitro* and then implanted into the body for bone regeneration, which requires a more extended period. In

[a]*Department of Biomedical Engineering, Chengde Medical University, Chengde, 067000, Hebei, China. E-mail: xushiqi@cdmc.edu.cn; qianglinhui@163.com; Tel: +86-13343396119; +86-17774937339*

[b]*Hebei International Research Center for Medical-Engineering, Chengde Medical University, Chengde, 067000, Hebei, China*

[c]*Chengde Medical Additive Manufacturing Technology Innovation Center, Chengde Medical University, Chengde, 067000, Hebei, China*

© 2024 The Author(s). Published by the Royal Society of Chemistry

Open Access Article. Published on 15 July 2024. Downloaded on 11/10/2025 11:29:51 AM. This article is licensed under a Creative Commons Attribution-NonCommercial 3.0 Unported Licence.

addition, there are many uncertainties in the *in vitro* culture of seed cells, all of which limit the clinical translation of bone tissue-engineered scaffolds.[19]

The *in situ* mineralization method, which has recently attracted considerable attention as a bone repair technique, has generated widespread interest due to its unique mechanism and potential advantages. Zhang *et al.*[20] developed an *in situ* mineralized composite hydrogel, utilizing endogenous bone alkaline phosphatase to catalyze the *in situ* conversion of calcium glycerophosphate and calcium carbonate incorporated within the hydrogel into hydroxyapatite nanocrystals. This composite hydrogel exhibits excellent biocompatibility and can be utilized for tooth restoration as well as the regeneration of complex tissues. Liu *et al.*[21] proposed an *in situ* mineralized PLGA/PSBMA hydrogel composite scaffold capable of efficiently releasing rhBMP-2. Their research demonstrated that this scaffold effectively facilitated the robust healing of critical-sized non-condylar bone defects in rats. Additionally, researchers have investigated an osteoinductive hybrid hydrogel membrane for *in situ* bone regeneration in hyperglycemic patients. This study involved incorporating a biomineralized calcium source onto the surface of the hybrid hydrogel, creating an osteoinductive microenvironment through the release of calcium ions. The results demonstrated that this membrane stimulated angiogenesis in a diabetic model and accelerated the effective repair of bone defect areas.[22]

The *in situ* mineralization method primarily simulates the natural bone mineralization process, aiming to fully utilize the physiological processes within the body and induce mineralization at the site of injury to promote the growth and repair of bone tissue, thereby reducing the need for external intervention.[23] This method not only reduces the patient's pain but also has the potential to shorten the recovery time and reduce the need for surgery and other exogenous treatments.[24] This method has many potential advantages, such as not requiring cell culture *in vitro* and directly implanting the prepared scaffold into the body. It utilizes the components of the *in vivo* microenvironment to induce bone cell growth, which can reduce unnecessary risks and provide a more innovative and effective option for bone tissue repair.

In summary, this study proposed an *in situ* mineralized, highly biocompatible bone tissue engineering scaffold. This scaffold utilizes bone-alkaline phosphatase in the *in vivo* microenvironment to catalyze the *in situ* mineralization of calcium sources within the bone tissue engineering scaffold. It achieves degradation and *in situ* mineralization of the scaffold while constructing an environment conducive to the growth of osteoblasts with high mechanical strength and similar microstructures as bone tissue, promoting bone induction and conduction.

2 Materials and methods

2.1 Materials

Polylactic acid–glycolic acid copolymer (PLGA 75 : 25, Jinan Daisan Biological Engineering Co., Ltd); hexafluoroisopropanol (HIFP, 99.5%, Aladdin); calcium glycerophosphate (CaG, 98%, Shanghai Yuanphen Biotechnology Co., Ltd); glycerin (ACS, ≥99.5%, Aladdin); alkaline phosphatase (ALP, activity > 1000 μ mg^{-1}, bovine intestinal, Shanghai Yuanphen Biotechnology Co., Ltd); Phosphate Buffered Saline (PBS, 0.2 mol L^{-1}, pH 9.0, Shanghai Yuanphen Biotechnology Co., Ltd).

2.2 Scaffold fabrication

2.2.1 Preparation of electrospinning solution. 0.8 g of PLGA was added to 9.2 g of HIFP, and the mixture was magnetically stirred at room temperature for 30 minutes until complete dissolution of PLGA occurred. The resulting solution, with a mass/volume ratio of 8% for PLGA, was designated as PLGA-8.

Then, the CaG powder was added to glycerin, heated, and stirred at 90 °C until the solution was dissolved entirely and became transparent, resulting in a series of CaG solutions with varying concentrations. One of the roles of glycerol is to promote the dissolution of calcium glycerophosphate, enabling its even distribution in the spinning precursor solution.

A specific volume of PLGA-8 solution was mixed and stirred with CaG solution to generate a series of PLGA/CaG composite solutions. The final composite solutions contained CaG additions of 0 wt%, 7.2 wt%, 15.8 wt%, 20.1 wt%, 23.8 wt% and 27.3 wt% (the mass percentage of CaG in the composite solution). The sample with a CaG addition of 0 was prepared as the control group for subsequent cell experiments.

2.2.2 Electrospinning. This study used electrospinning technology to prepare PLGA bone tissue engineering scaffolds. The electrospinning equipment comprises a high-voltage power supply, a collector, and an injection pump. The needle is connected to the positive pole of the high-voltage power supply, while the negative pole is connected to the collector to create a high-voltage electric field. Electrospinning takes place in an enclosed environment.[25]

The PLGA/CaG mixed solution was first stirred in the vortex again. Then, the prepared electrospinning solution was drawn into a 10 mL disposable syringe with a needle diameter of 0.8 mm. The syringe was left to stand for 5 minutes and lightly tapped to expel bubbles in the tube. After that, electrospinning was performed under a series of constant parameters: flow rate at 1 mL h^{-1}, adjusting the distance between the needle tip and the collector, controlling the voltage, and performing at room temperature. Using aluminum foil as a collector, the collected fiber membrane is vacuum-dried for at least 24 hours to remove residual solvents. For subsequent characterization and analysis, the fibrous membranes were prepared from PLGA/CaG composite solutions with CaG concentrations of 0 wt%, 7.2 wt%, 15.8 wt%, 20.1 wt%, 23.8 wt%, and 27.3 wt% were respectively designated as PLGA/CaG-0, PLGA/CaG-7.2, PLGA/CaG-15.8, PLGA/CaG-20.1, PLGA/CaG-23.8, and PLGA/CaG-27.3.

2.3 Characterization of the scaffolds

2.3.1 Scanning electron microscope (SEM) and energy-dispersive X-ray spectroscopy (EDS). The morphology of the samples was observed using a field emission scanning electron microscope (FE-SEM, TESCAN MIRA LMS) with an accelerating

Open Access Article. Published on 15 July 2024. Downloaded on 11/10/2025 11:29:51 AM.
This article is licensed under a Creative Commons Attribution-NonCommercial 3.0 Unported Licence.

voltage of 15 kV and a working distance of 10.2 mm. Cut the fiber membrane into 1 cm × 1 cm pieces, attach them directly to the conductive adhesive on the metal sample holder, and then spray them with gold for observation. Scan the sample while conducting elemental spectroscopic analysis (EDS) on it.

2.3.2 X-ray diffraction (XRD). The phases of the fiber scaffold were studied using the Rigaku/SmartLab SE diffractometer and a Cu radiation source by XRD. The scanning range of the 2theta angle is from 5 to 90°, and the scanning speed is 10° per minute. The peak identification of crystal phases refers to the International Center for Diffraction Data (ICDD).

2.4 *In vitro* degradation

To evaluate the *in vitro* degradation of the PLGA/CaG-23.8 fiber scaffold, it was immersed in a phosphate-buffered saline (PBS) solution at 37 °C and pH 7.4. Place the fiber scaffold in a vacuum-drying oven and dry it to a constant weight. Record the initial mass as m_0. These pieces were placed in a 24-well plate containing PBS, replacing the solution every 5 days. After 7, 14, and 21 days of immersion, the samples were removed, rinsed three times with deionized water, dried, and weighed to obtain the final mass m_1. The mass loss rate was calculated using the formula: mass loss rate $= (m_0 - m_1)/m_0 \times 100\%$.[26]

2.5 *In vitro* simulation of *in situ* mineralization

2.5.1 Preparation of ALP solution. Prepare (0.1 mol L^{-1}, pH 9.0) PBS phosphate buffer solution. According to the method of Chen *et al.*,[27] 2 mg of ALP was dissolved in 10 mL of PBS buffer solution and gently shaken to dissolve the ALP in the buffer solution completely. The prepared enzyme solution was sealed and stored in the refrigerator and should be used within 3 hours.

2.5.2 *In situ* mineralization. *In vitro* simulation of *in situ* mineralization was conducted using PLGA/CaG-23.8 fiber membranes. The experiment will be conducted on a 24-well plate. First, the 24-well plate was cleaned three times with a PBS buffer solution (0.1 mol L^{-1}, pH 9.0). The PLGA/CaG-23.8 fiber membrane was cut into pieces measuring 1 cm × 1 cm and placed in the 24-well plate. The fiber membrane was washed three times with the buffer solution to remove any residual solvent. In a 24-well plate containing a fiber membrane, 2 mL of enzyme solution was added, and the plate was placed in an incubator at 37 °C for 1 d, 3 d, 5 d, and 7 d. The membrane was washed with PBS buffer solution three times and dried in a drying oven for 12 hours. Subsequently, the mineralized fiber membrane was labeled A-1, A-3, A-5, and A-7, respectively, and stored at room temperature for subsequent characterization and *in vitro* cell experiments.

2.6 Mechanical properties

In a room-temperature environment, the compressive mechanical properties of the mineralized fiber scaffolds were characterized at a compression rate of 0.5 mm min^{-1} with a mechanical load of 100 N. Mechanical tests were performed on PLGA/CaG-23.8 scaffolds mineralized for 3 and 7 days. All samples were cut into rectangular specimens measuring 6 mm × 5 mm × 4 mm, with three parallel groups for each scaffold type.

2.7 Evaluation of biocompatibility

We used MC3T3-E1 mouse embryonic osteoblasts to evaluate the fiber scaffold's cytotoxicity, adhesion, and proliferation properties. Prepare DMEM high-glucose culture medium (10% fetal bovine serum and 1% penicillin–streptomycin solution), revive MC3T3-E1 cells (mouse embryonic osteoblast progenitor cells), and culture them in a 37 °C incubator with 95% relative humidity and 5% CO_2 for subculture. The experiment had four groups: the PLGA/CaG-23.8 group, the PLGA-8 group, the control group, and the blank medium group. PLGA/CaG-23.8 and PLGA-8 fiber membranes were punched into 6 mm diameter discs using a punch and then sterilized with UV light for 2 hours. They were placed in 96-well plates as the PLGA/CaG-23.8 group and the PLGA-8 group. Take a certain amount of cell suspension and adjust the cell concentration to 8×10^4 cells per mL. Add 100 μL of the cell suspension to each group of PLGA/CaG-23.8, PLGA-8, and the control group. Add an equal volume of cell complete culture medium to the blank medium group. Place all samples in the incubator.

2.7.1 Cell toxicity test. After 48 hours of culture for each group, cytotoxicity was assessed using the Cell Counting Kit-8 (CCK-8) assay. The optical density (OD) of the samples was measured at 450 nm using a microplate reader. Each experiment was repeated three times. The toxicity of the material was evaluated based on the relative growth rate (RGT) of the cells.[28] The calculation formula is RGT = [*A*(experimental) − *A*(blank medium)]/[*A*(control) − *A*(blank medium)] × 100. The classification of cytotoxicity is shown in Table 1.

2.7.2 Cell proliferation and adhesion properties. Each group was cultured for 1 d, 7 d, and 14 d separately. After the culture was completed, the original culture medium was aspirated, and the cells were washed with sterile PBS three times. Each well was added with 100 μL of 4% paraformaldehyde to fix the cells, and the fixation time was 10 minutes. The sample is washed with PBS thrice, each for 30 seconds. Add a 0.5% solution of Triton X-100 (Wuhan Saiwei Biological Technology Co., Ltd) to permeabilize the cells, incubate at room temperature for 5 minutes, and wash the sample with PBS three times, each time for 30 seconds. Take 50 μL of the freshly prepared TRITC-Phallodin staining working solution and add it onto the surface of the sample membrane. Incubate at room temperature in the dark for 30 minutes. Wash the sample with PBS three times, each for 30 seconds; Add 50 μL of DAPI solution (Solarbio

Table 1 Cytotoxicity grading criteria

Cellular toxicity grade	Relative cell proliferation rate (%)	Evaluation
0	≥100	Noncytotoxic
1	75–99	Mild cytotoxicity
2	50–74	Moderate cytotoxicity
3	≤49	Severe cytotoxicity

 © 2024 The Author(s). Published by the Royal Society of Chemistry

Open Access Article. Published on 15 July 2024. Downloaded on 11/10/2025 11:29:51 AM.
This article is licensed under a Creative Commons Attribution-NonCommercial 3.0 Unported Licence.

Biotechnology Co., Ltd, 100 nM) and incubate in the dark for 1 minute to counterstain the cell nuclei. Wash the sample with PBS three times, each time for 30 seconds. After culturing the cells for 1 day, the scaffold was treated with platinum spray, and cell proliferation was observed using SEM. Cell morphology on the membrane was observed using a fluorescence microscope after culturing for 1 d, 7 d, and 14 d.

2.8 Evaluation of *in vitro* osteogenic performance

The MC3T3-E1 mouse embryonic osteoblasts were used to evaluate osteoblasts' *in situ* mineralization and differentiation on the fiber scaffold. The cell culture method is described in section 2.5. The experiment had three groups: PLGA/CaG-23.8 group, PLGA-8 group, and A-7 group.

2.8.1 Qualitative and quantitative assessment of ALP. After 7 d, 14 d, and 21 d of cell culture, the culture medium was aspirated, and the cells were gently washed with sterile PBS three times. Then, each well was treated with 100 μL of 4% paraformaldehyde to fix the cells for 30 minutes before being washed with PBS three times. 50 μL of the freshly prepared BCIP/NBT staining working solution is added to each well. The tubes are incubated in the dark at room temperature for 20 hours. The staining working solution is then aspirated, and the wells are washed twice with ultrapure water to terminate the staining reaction. Finally, the tubes are allowed to air dry, and the colonies are observed and photographed using a stereomicroscope.

After 7 d, 14 d, and 21 d of cell culture, the culture medium was aspirated, and the cells were gently washed with sterile PBS three times. Each well was then incubated with 55 μL of cell lysis solution for 3 minutes to lyse the cells. Subsequently, 50 μL of the lysate was transferred to a blank 96-well plate, and standard and blank wells were set up. Following Table 2 instructions, each well was sequentially added with the following reagents, and the OD value at 520 nm was measured using a microplate reader.

2.8.2 Qualitative and quantitative analysis of calcific nodules. After 7 d, 14 d, and 21 d of cell culture, the culture medium was aspirated, and the cells were gently washed with sterile PBS three times. Then, each well was treated with 100 μL of 4% paraformaldehyde to fix the cells for 30 minutes before being washed with PBS three times. Add 50 μL of alizarin red dye to each well and incubate at room temperature for 10 minutes. Remove the stained working solution and wash it with ultrapure water several times to eliminate any remaining alizarin red dye. Allow it to air dry at room temperature, and observe and photograph the specimen using an optical microscope for qualitative detection data.

In each well, add 120 μL of the 10% chloro-hexadecyl-pyridinium chloride solution prepared immediately, and incubate the plate at 37 °C in a thermo-shaker for 10 minutes. Remove 100 μL of the solution from each well and transfer it to a blank well. Use a microplate reader to measure the absorbance at 562 nm for quantitative detection data of cellular calcium nodules.

2.8.3 Osteogenic-related protein detection. After 7 d, 14 d, and 21 d of cell culture, OCN, OPN, and Runx2 expression were detected through immunofluorescence staining. After cell culture, the cells were fixed according to Method 2.6.2. Then, 10% bovine serum albumin (BSA) solution was added to each well and incubated for 2 hours. The wells were washed with PBS three times, each for 3 minutes. Add the diluted primary antibody, incubate at 4 °C overnight, and wash three times with PBS containing Tween-20 (10%) for 3 minutes each time after incubation. Add the diluted FITC-labeled secondary antibody, incubate at room temperature in the dark for 12 hours, and wash three times with PBS containing Tween-20 (10%) for 3 minutes each time. Add DAPI solution and incubate in the dark for 5 minutes to counterstain the cell nucleus. Wash with PBS three times. A fluorescence microscope was used to observe the expression of OCN, OPN, and Runx2 in MC3T3-E1 cells.

2.9 Statistical analyses

In this study, each experimental section was repeated three times, and the result of each study was expressed as mean ± standard deviation. One-way analysis of variance (ANOVA) was used to analyze statistical differences between the experimental groups. The difference was considered to be statistically significant when $P < 0.05$.

3 Results and discussion

The process of preparing and *in situ* mineralizing the scaffold is illustrated in Fig. 1. Firstly, a precursor solution is prepared by adding a certain amount of calcium phosphate and thoroughly stirring to ensure complete dissolution throughout the solution. Secondly, we utilized electrospinning technology to fabricate fiber scaffolds. By applying a high-voltage electric field, the solution is drawn into a filament and collected on the corresponding collector. The voltage and the distance between the

Table 2 Reagent additive for quantification of ALP activity

	Blank	Standard	PLGA/CaG-23.8	PLGA-8	A-7
Double-distilled water (μL)	5				
0.1 mg per mL phenol standard application (μL)		5			
Buffer solution (μL)	50	50	50	50	50
Thoroughly mix the solution in a water bath at 37 °C for 15 minutes					
A chromophore (μL)	150	150	150	150	
Measure the absorbance at 520 nm using a microplate reader					

Open Access Article. Published on 15 July 2024. Downloaded on 11/10/2025 11:29:51 AM.
This article is licensed under a Creative Commons Attribution-NonCommercial 3.0 Unported Licence.

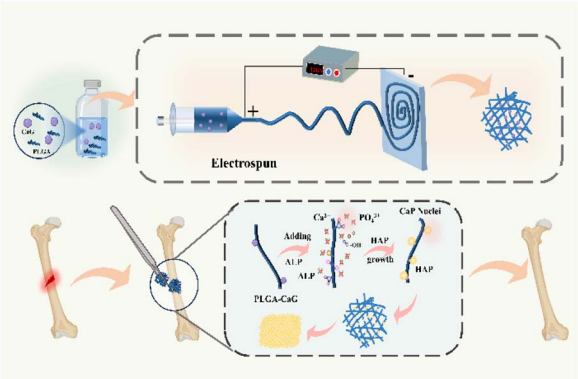

Fig. 1 Preparation and *in situ* mineralization process of bone tissue engineering scaffold.

needle tip and the collector are adjusted to regulate the morphology and diameter of the fibers. The prepared scaffold is implanted into the body, and ALP catalyzes the mineralization of the scaffold in the bone microenvironment, ultimately facilitating bone defect repair.

3.1 Scanning electron microscope (SEM) and energy-dispersive X-ray spectroscopy (EDS)

3.1.1 The effect of CaG concentration on the morphology of fiber membrane. SEM characterization was performed to investigate the surface morphology of nanofiber membranes obtained from 8 wt% PLGA blend solutions with different CaG additions (7.2 wt%, 15.8 wt%, 20 wt%, 23.8 wt% and 27.3 wt%), under the same electrospinning conditions. The results indicated that the PLGA/CaG composite nanofibers exhibited a three-dimensional porous network formed by randomly non-oriented, filamentous electrospun fibers creating interconnected pores. This structure is consistent with the fiber architecture prepared by Wang *et al.*[29] The SEM images in Fig. 2(a1)–(e1) clearly demonstrate that when the CaG concentration in the scaffold is low, the fibers are uniform in diameter and free from adhesion. As the CaG concentration decreases, the fibers become finer. With an increase in concentration, the fibers thicken, and a slight stringing phenomenon appears on the scaffold surface. Moreover, as the concentration increases further, there is a decrease in the uniformity of fiber diameter and an increase in adhesion between fibers (as shown in Fig. 2(e1)). This indicates that CaG concentration significantly affects the morphology of electrospun scaffolds.

The EDS analysis (Fig. 2(a2)–(e2)) was conducted to detect the elements C, O, P, and Ca within the fibers. The EDS results indicate that the Ca content increases with an increase in CaG addition. The fiber morphology is relatively better when the Ca content is 5.48 wt% or lower, but once it reaches 6.28 wt%, a sticky phenomenon occurs on the fiber surface. During the adhesion process, fibers can form irregular aggregates, resulting in significant variations in fiber diameter across different regions. This increases the range of fiber diameter distribution and leads to the formation of non-uniform pores. A broad fiber diameter distribution and uneven pore structure can hinder cell attachment and spread on the scaffold, affecting cell proliferation.[30] Furthermore, the non-uniform pore structure can impede the transport of nutrients, limiting cell growth.[31] Therefore, we selected the PLGA/CaG-23.8 fiber scaffold in this study, which exhibited higher CaG concentration and better morphology, for subsequent experiments.

3.1.2 The effect of distance on the fiber scaffold morphology. When preparing fiber scaffolds, the distance between the needle tip and the receiver can impact the shape of the fiber scaffold.[32–34] This study controlled the addition rate of CaG at 23.8 wt% and the high-pressure voltage at 12.5 kV. It investigated the influence of distance parameters on the morphology of the final fiber scaffold. The experimental results, shown in Fig. 3(a1)–(e1), indicate that the distance change directly affects the electrospun fibers' morphology and structure. At shorter distances (Fig. 3(a1)), the fibers exhibit uneven thickness and irregular shapes, with a noticeable cross-linking. As the distance increases, the spinning liquid is more likely to split in the air evenly, forming independent fiber structures.[35] At a distance of 20 cm, the fiber morphology presents its optimal state, with an average fiber diameter of 2.4 ± 0.25 μm. However, when the distance was further increased to 29 cm, the fibers received by the collector became sparse. This may be attributed to the fact that the needle tip was too far away from the collector, resulting in ineffective reception of some fibers.

The diameter distribution of fibers at different distances is shown in Fig. 3(a2)–(e2), and it is observed that the diameter of fibers decreases as the distance increases. The average diameter of the fibers is maximum at 2.7 ± 0.72 μm when the distance between the needle tip and the collector is 13 cm. However, when the distance is increased to 29 cm, the average diameter of the fibers reduces to 1.8 ± 0.50 μm. Among them, at a distance of 20 cm, there is a minor standard deviation of fiber diameter (0.25 μm), indicating that the fibers are more uniform in diameter at this distance. Therefore, it can be concluded that an optimal distance between the needle tip and collector would be 20 cm.

3.1.3 The influence of voltage on fiber morphology. The voltage of the electric field is an essential factor that affects the morphology of the fibers in the electrospinning process.[36] In this study, the CaG addition rate was controlled at 23.8 wt%, the distance from the nozzle to the collector was set at 20 cm, and the voltage was adjusted within the range of 8.5–16.5 kV to investigate the effect of voltage on electrospun fiber morphology. The experimental results demonstrate that changes in voltage significantly impact the morphological characteristics of electrospun fibers. The fibers exhibit less regular morphology and uneven distribution, as shown in Fig. 4(a1)–(e1) at lower voltages, and the fiber diameter is relatively larger. For instance, when the voltage is 8.5 kV, the average diameter reaches 2.9 ± 0.57 μm (Fig. 4(a2)), and fiber diameters are uneven. Fibers may also show flat and non-fiberized features between voltages of 8.5 and 10.5 kV; however, finer fiber structures are formed at higher voltage conditions (such as the fibers at a voltage of 16.5 kV with an average diameter of 1.2 ± 0.25 μm), exhibiting more regular morphology and even distribution. When the voltage is set to

 © 2024 The Author(s). Published by the Royal Society of Chemistry

Open Access Article. Published on 15 July 2024. Downloaded on 11/10/2025 11:29:51 AM.
This article is licensed under a Creative Commons Attribution-NonCommercial 3.0 Unported Licence.

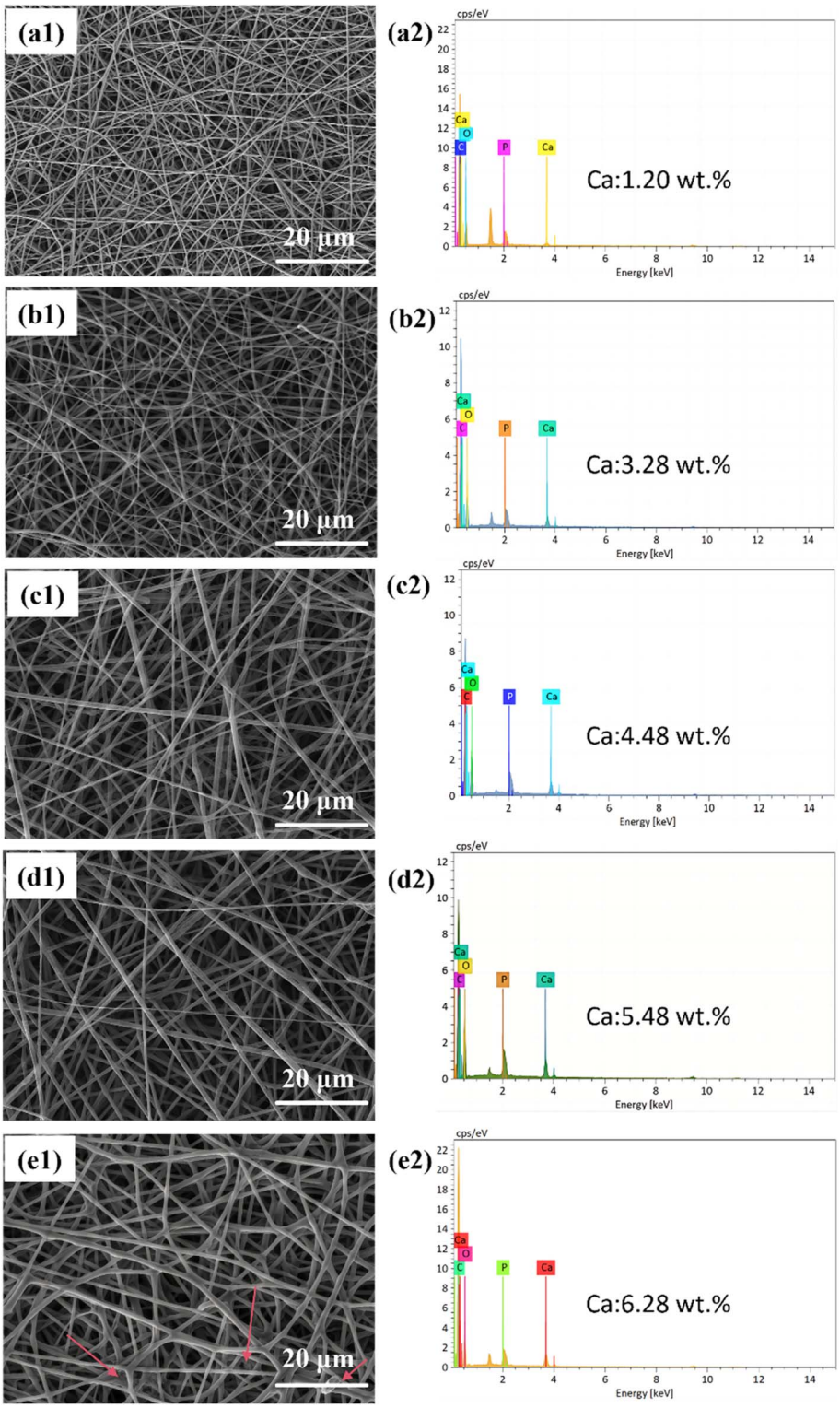

Fig. 2 (a1)–(e1) Shows SEM morphological images of fiber scaffolds with CaG additions at concentrations of 7.2, 15.8, 20.1, 23.8, and 27.3 wt%; (a2)–(e2) displays EDS energy dispersive spectra corresponding to different CaG concentrations of the fiber scaffolds.

12.5 kV, the fiber morphology improves significantly with a relatively uniform diameter averaging at 2.2 ± 0.16 μm without bead-like phenomena observed. Therefore, a voltage of 12.5 kV is selected as the optimal choice.

3.2 *In vitro* degradation

The degradation performance of the PLGA/CaG-23.8 fiber membrane was evaluated in this study. As shown in Fig. 5, the fiber membrane exhibited a mass loss of 7.21% after 7 days of

Open Access Article. Published on 15 July 2024. Downloaded on 11/10/2025 11:29:51 AM.
This article is licensed under a Creative Commons Attribution-NonCommercial 3.0 Unported Licence.

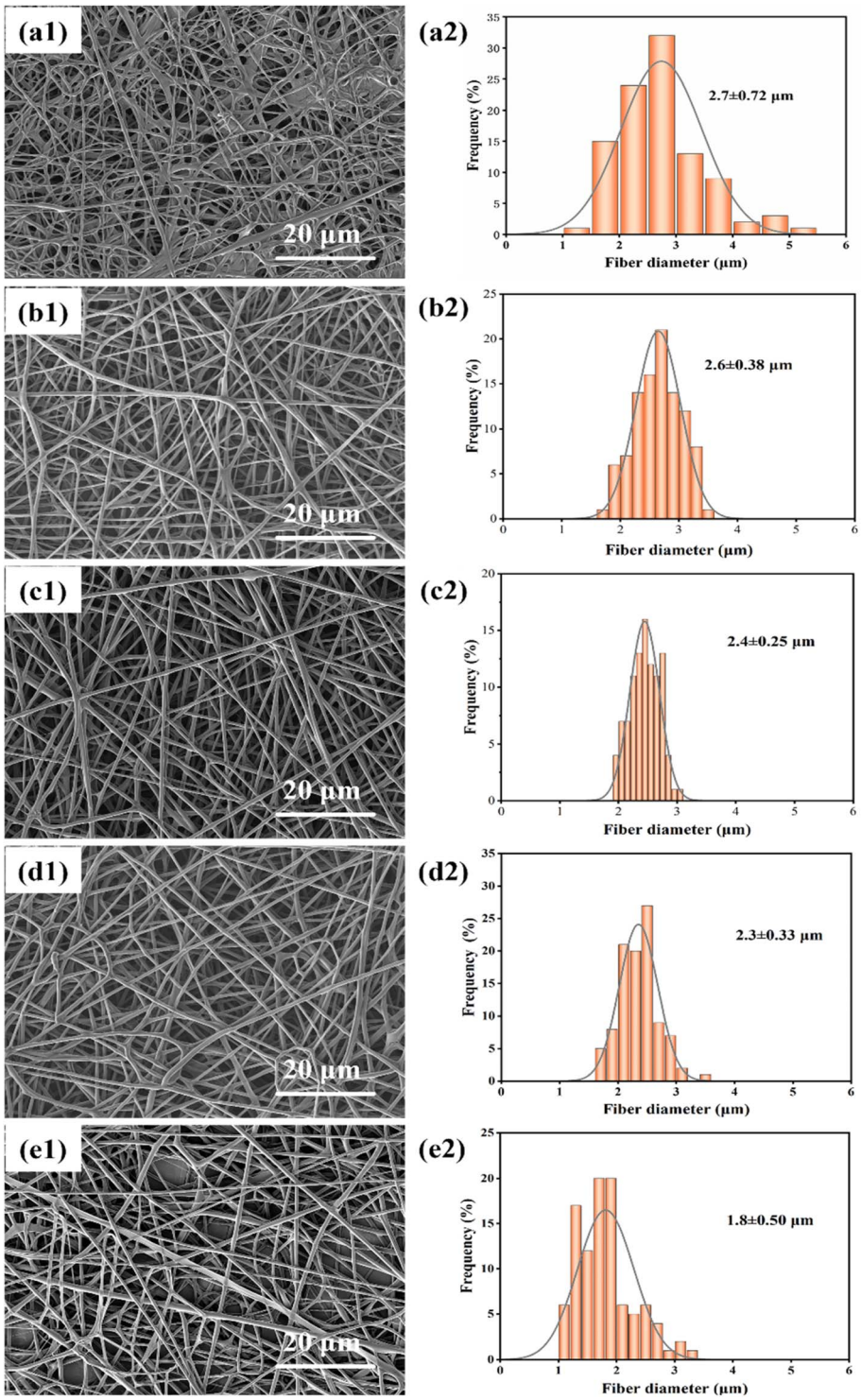

Fig. 3 (a1)–(e1) Show SEM images of fibers spun at distances of 13 cm, 17 cm, 20 cm, 25 cm, and 29 cm, respectively; (a2)–(e2) show the diameter distribution of fibers at different distances.

degradation in PBS. As time progressed, the degradation rate increased, with a mass loss of 10.36% at 14 days and 15.48% at 21 days, indicating significant degradation and dissolution of the molecules within the scaffold. In the early stages of degradation, the mass loss rate was not particularly high. However, as degradation continued and small, soluble molecules were produced, the mass loss rate significantly accelerated.

3.3 *In vitro* simulation of *in situ* mineralization

3.3.1 SEM morphological characterization. The SEM image of the PLAG/CaG-23.8 fiber membrane utilizing ALP to induce simulated *in situ* mineralization is shown in Fig. 6. By adjusting the mineralization time (1 d, 3 d, 5 d, 7 d), we can investigate the growth and morphology of calcium phosphate compounds on

 © 2024 The Author(s). Published by the Royal Society of Chemistry

Open Access Article. Published on 15 July 2024. Downloaded on 11/10/2025 11:29:51 AM.
This article is licensed under a Creative Commons Attribution-NonCommercial 3.0 Unported Licence.

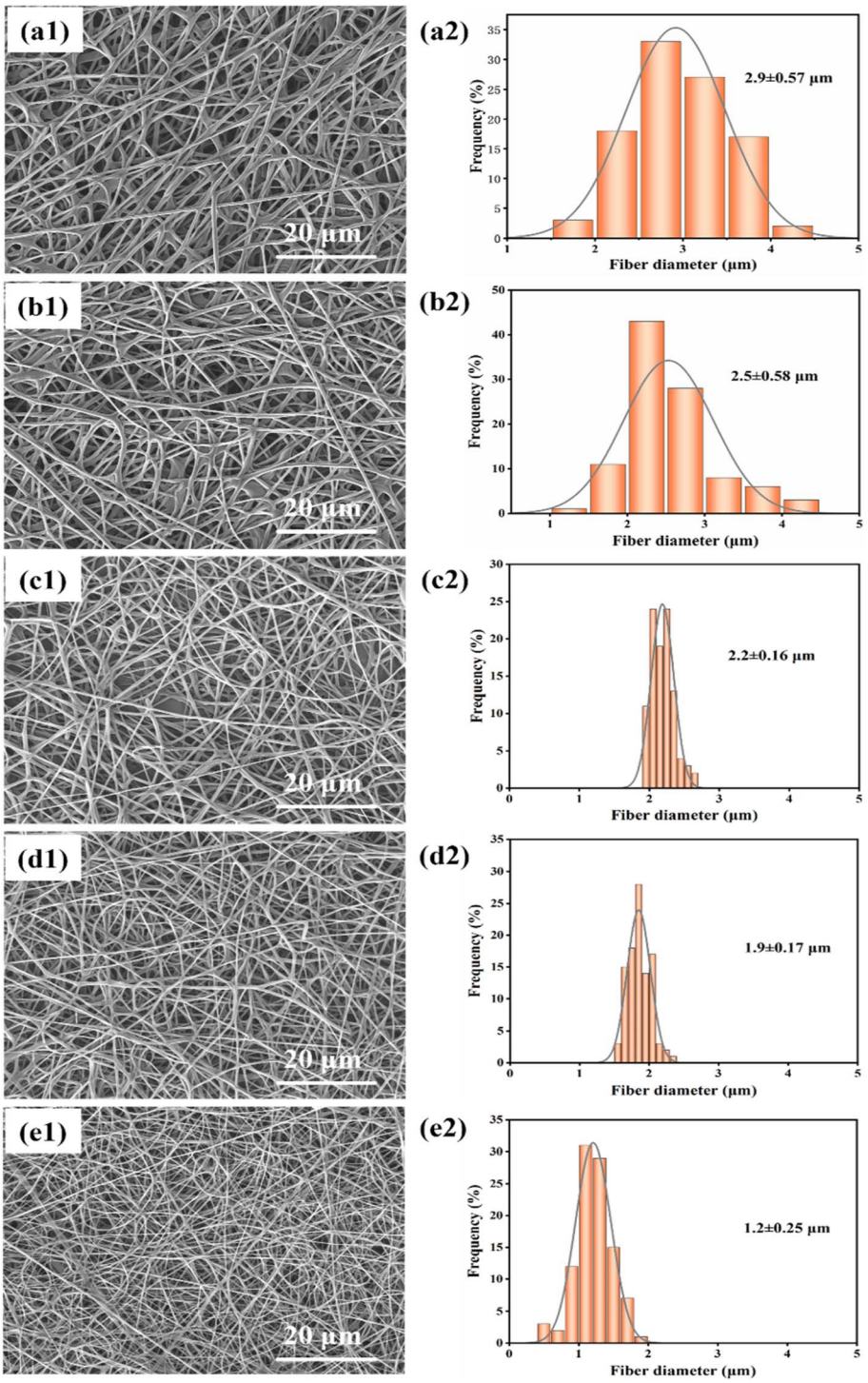

Fig. 4 (a1)–(e1) Show the SEM images of the electrospun fibers at different voltages of 8.5 kV, 10.5 kV, 12.5 kV, 14.5 kV, and 16.5 kV; (a2)–(e2) show the diameter distribution of the fibers at different voltages.

the fiber membrane after mineralization. As shown in Fig. 6(a1)–(d1), the mineralization forms a granular structure, gradually growing on the fiber surface and eventually completely wrapping the fiber, which is consistent with the morphology of the fiber membrane obtained in previous studies after mineralization.[29,37] As shown in Fig. 6(a2)–(d2), the high-resolution SEM images of the mineralized tissue exhibit a honeycomb-like distribution and irregular shape, which is more conducive to cell adhesion and proliferation.[38,39] The duration of mineralization has a significant impact on the growth of mineral deposits.[40] As shown in Fig. 6(a1), only a tiny amount of mineralization was observed on the fibers after 1 day, and the filamentous structure of the fibers was clearly visible. With the prolongation of mineralization time, the amount of

Open Access Article. Published on 15 July 2024. Downloaded on 11/10/2025 11:29:51 AM.
This article is licensed under a Creative Commons Attribution-NonCommercial 3.0 Unported Licence.

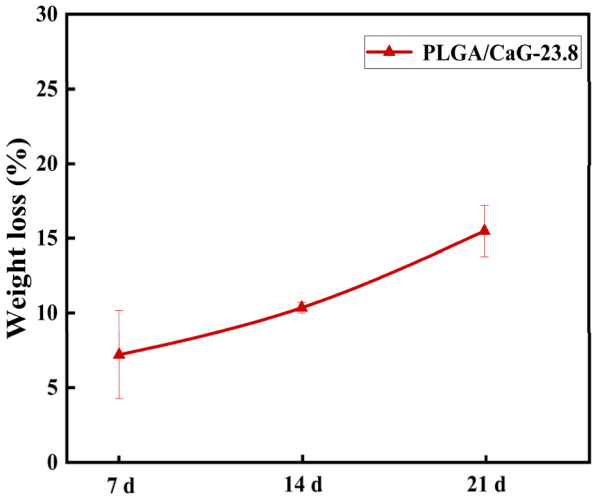

Fig. 5 The mass loss rates of the PLGA/CaG-23.8 fiber scaffold after degradation in PBS for 7, 14, and 21 days.

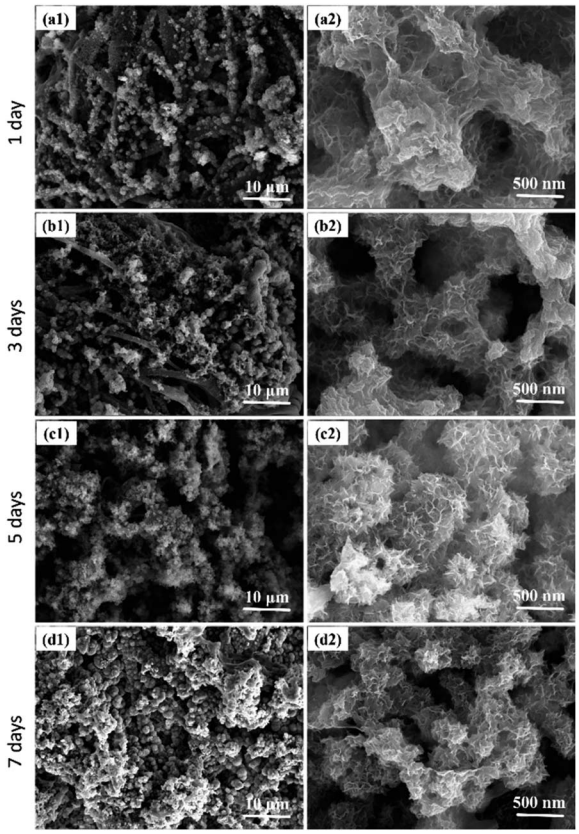

Fig. 6 Shows SEM images of enzyme-induced mineralization of fiber scaffold structures: (a1) and (a2) represent mineralization after 1 day; (b1) and (b2) represent mineralization after 3 days; (c1) and (c2) represent mineralization after 5 days; and (d1) and (d2) represent mineralization after 7 days.

mineralization gradually increased, as shown in Fig. 6(d1). Eventually, it completely wrapped around the fibers, leaving only granular mineralization on the fiber surface, making it difficult to recognize the original fiber structure.

The results mentioned above indicate that enzymatic catalysis can facilitate the mineralization of calcium phosphate within the fibers. The quantity of mineral deposits and the fibrous membrane's morphology can be controlled by extending the mineralization time. With sufficient enzyme content, prolonged mineralization time leads to an increased amount of mineral deposits on the fiber surfaces, thereby enhancing the mechanical strength of the bone tissue engineering scaffold.[41] As the scaffold degrades, the fibrous membrane is gradually replaced by mineral deposits, forming a structure composed entirely of minerals.

3.3.2 XRD characterization of minerals. We characterized the minerals using EDS and XRD to analyze the properties of the minerals formed after the mineralization of the fibrous scaffold. The structure diagram of the PLGA/CaG fiber scaffold is presented in Fig. 7(a). Fig. 7(b) shows the morphology of the mineralized material on the fiber scaffold, which appears as granules or microspheres with a honeycomb surface. Fig. 7(c) presents the EDS energy spectrum analysis of the minerals, detailing the content of C, O, P, and Ca elements. The results indicate that the minerals contain a substantial amount of Ca, with a mass percentage reaching 26.65 wt%, comparable to the Ca content in HAP obtained after the hydrolysis of CaG.

We conducted an XRD analysis to analyze the mineralization properties further, as shown in Fig. 7(d). Some characteristic peaks appeared at 2θ angles of 31.773° and 45.305°, consistent with the standard diffraction peaks of HAP (JCPDS 09-0432).[42] This result confirms that the mineralization is composed of hydroxyapatite.

Based on the above results, it can be concluded that APL can catalyze the mineralization of CaG added to the fiber, ultimately forming a component similar to hydroxyapatite found in bones. This process helps promote bone induction and conduction.[43]

3.4 Mechanical properties testing

The mechanical properties of fiber scaffolds are crucial for bone tissue repair. In this study, the compressive mechanical

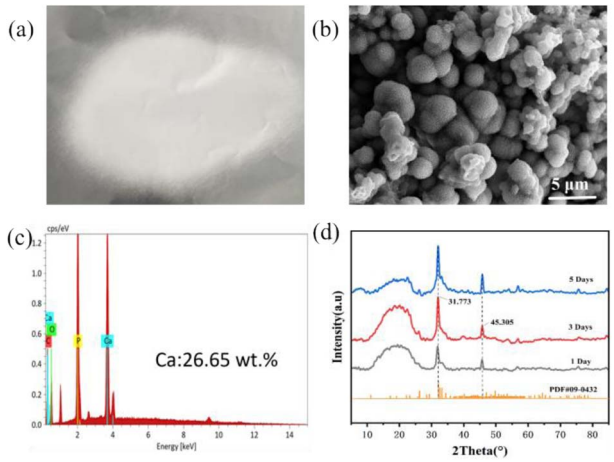

Fig. 7 (a) PLGA/CaG fiber scaffold; (b) SEM image of the mineral; (c) EDS analysis of the mineral; (d) XRD analysis of the mineral.

 © 2024 The Author(s). Published by the Royal Society of Chemistry

Open Access Article. Published on 15 July 2024. Downloaded on 11/10/2025 11:29:51 AM.
This article is licensed under a Creative Commons Attribution-NonCommercial 3.0 Unported Licence.

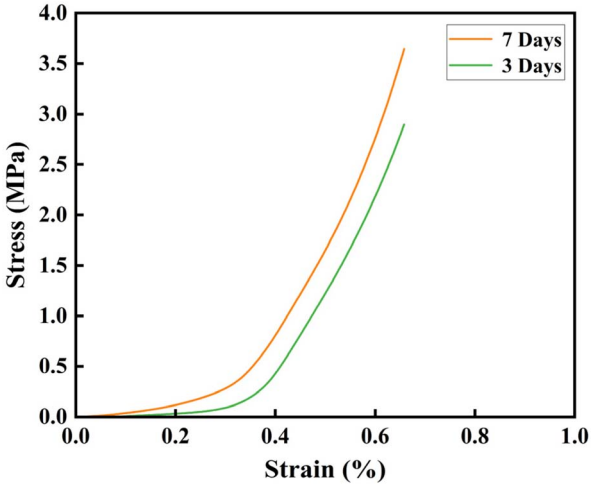

Fig. 8 Compressive stress–strain curves for PLGA/CaG fiber scaffolds after 3 and 7 days of mineralization.

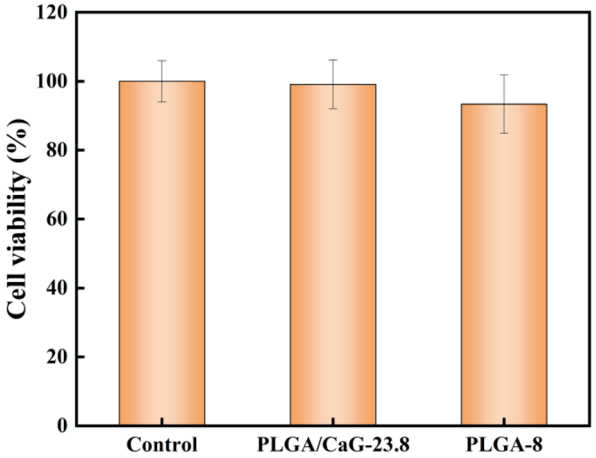

Fig. 9 Cell viability results of MC3T3-E1 cells cultured on PLGA/CaG-23.8 and PLGA-8 scaffolds.

properties of the mineralized PLGA/CaG-23.8 fiber scaffold were evaluated. The stress–strain curves are presented in Fig. 8. Compared to scaffolds mineralized for 3 days, those mineralized for 7 days exhibited significantly higher compressive strength and modulus. Specifically, after 3 days of mineralization, the compressive strength and modulus were 3.23 MPa and 8.06 MPa, respectively. These values increased to 3.64 MPa and 8.45 MPa after 7 days of mineralization. As confirmed by previous SEM and EDS analyses, this improvement can be attributed to the increased deposition of hydroxyapatite on the fiber surfaces, forming a more robust structural network that distributes the load more effectively.

3.5 Biocompatibility assessment

3.5.1 Cytotoxicity. The activity and migration of cells on biomaterials are crucial for the subsequent bone repair process. In this study, the growth of MC3T3-E1 cells on the non-mineralized scaffold was assessed using the CCK-8 assay kit. The experimental results showed that after co-culturing cells with the scaffold for 48 hours, the cell survival rates of the control group, PLGA/CaG-23.8 group, and PLGA-8 group were 100 ± 6.02%, 99.08 ± 7.05%, and 93.38 ± 8.55%, respectively (Fig. 9). Among these groups, the cell survival rate of the PLGA/CaG-23.8 group was significantly higher than that of the PLGA-8 group and very close to the survival rate of the control group. By comparing cell viability with the cytotoxicity classification table, the results showed that the viability of cells cultured on both PLGA/CaG-23.8 and PLGA-8 exceeded 90%. Therefore, introducing CaG did not induce toxicity, and the fibrous membranes maintained excellent biocompatibility.

3.5.2 Cell proliferation and adhesion properties. The cell adhesion was observed using SEM, and the results are shown in Fig. 9. As depicted in Fig. 10(a), cells on the PLGA-8 fibrous scaffold mainly exhibited a spherical shape, indicating incomplete adhesion to the scaffold surface. In contrast, significant differences were observed in the SEM images of the PLGA/CaG-23.8 scaffold compared to the PLGA-8 scaffold, as shown in Fig. 10(b), a large number of honeycomb structures formed on the surface of the fibers, which is consistent with the structures formed during *in vitro* mineralization using ALP. This phenomenon may be attributed to the secretion of ALP by MC3T3-E1 cells during culture, which catalyzes the mineralization of CaG within the scaffold.[44] Additionally, the arrows in Fig. 10(b) clearly indicate areas where cell spreading is evident. These results suggest cells can adhere to the PLGA/CaG-23.8 scaffold and catalyze its *in situ* mineralization.

The scaffolds were stained to evaluate cell adhesion and spreading on the PLGA-8 and PLGA/CaG-23.8 fibrous scaffolds. The experimental results are shown in Fig. 11. After 48 hours of cell culture, cells were observed to spread well on both the PLGA-8 and PLGA/CaG-23.8 scaffolds. Compared to the PLGA-8 scaffold, the PLGA/CaG-23.8 scaffold exhibited a higher cell density and more extensive cell distribution. These results indicate that the PLGA/CaG-23.8 scaffold provides a more favorable environment for cell adhesion.

3.6 Evaluation of *in vitro* osteogenic performance

3.6.1 Qualitative and quantitative assessment of ALP. ALP is an early product of cell osteogenic differentiation.[45] During the experiment, we used ALP activity assays to quantitatively and qualitatively evaluate the osteogenic differentiation potential of PLGA/CaG-23.8, A-7, and PLGA-8 scaffolds.[46] In the qualitative assay, cells were stained with ALP at 7 d, 14 d, and

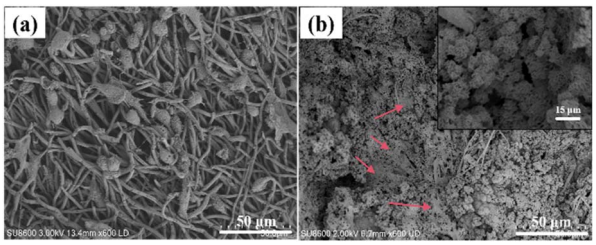

Fig. 10 SEM images of MC3T3-E1 cells after culturing on the scaffold, (a) PLGA-8, (b) PLGA/CaG-23.8.

Open Access Article. Published on 15 July 2024. Downloaded on 11/10/2025 11:29:51 AM.
This article is licensed under a Creative Commons Attribution-NonCommercial 3.0 Unported Licence.

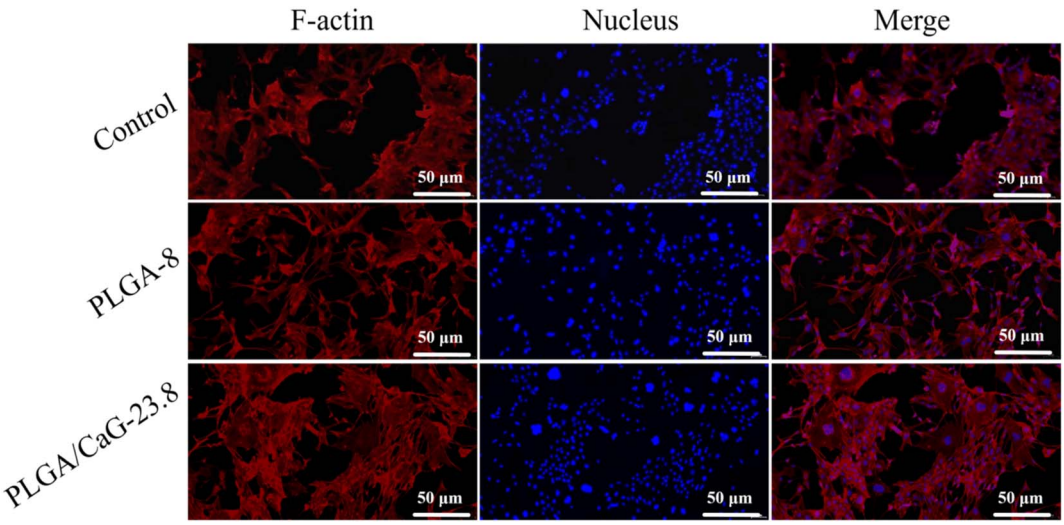

Fig. 11 Shows fluorescence staining images of the nucleus and cytoskeleton of MC3T3-E1 cells cultured on PLGA/CaG-23.8 and PLGA-8 for 48 hours.

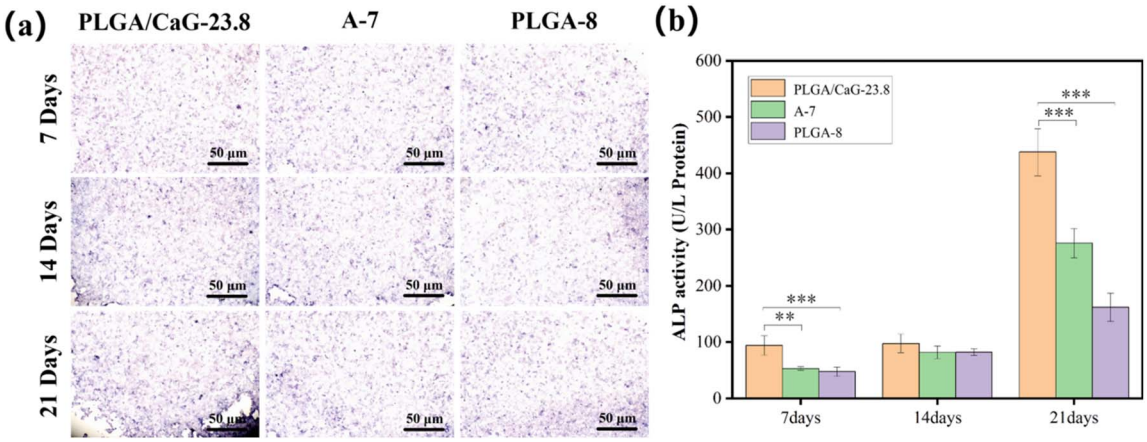

Fig. 12 Shows (a) ARS staining images and (b) quantitative analysis of calcium nodules in MC3T3-E1 cells cultured on PLGA/CaG-23.8, A-7, and PLGA-8 scaffolds for 7, 14, and 21 days (**$p < 0.01$, ***$p < 0.001$).

21 d. A transparent purple reaction was observed in Fig. 12(a), especially in the PLGA/CaG-23.8 fiber scaffold. Over time, the color intensity increased, indicating ALP activity in MC3T3-E1 osteoblasts across all three scaffold groups. Notably, the PLGA/CaG-23.8 fibrous scaffold exhibited higher ALP activity compared to the others.

Table 3 The ALP and OD values of cells cultured on different scaffolds at days 7, 14, and 21

		ALP (U L^{-1})	OD562
7 d	PLGA/CaG-23.8	93.613 ± 17.211	0.161 ± 0.004
	A-7	52.493 ± 3.154	0.128 ± 0.005
	PLGA-8	46.952 ± 8.315	0.119 ± 0.004
14 d	PLGA/CaG-23.8	97.113 ± 16.692	0.206 ± 0.006
	A-7	81.365 ± 11.374	0.211 ± 0.003
	PLGA-8	81.656 ± 5.955	0.222 ± 0.010
21 d	PLGA/CaG-23.8	437.445 ± 41.564	0.450 ± 0.008
	A-7	275.591 ± 26.086	0.344 ± 0.019
	PLGA-8	161.884 ± 25.301	0.347 ± 0.007

Table 3 and Fig. 12(b) present the ALP values after culturing cells in different groups for 7, 14, and 21 days, clearly demonstrating the differences among the groups over time. ALP enzyme activity levels were measured in cells cultured for 7 d, 14 d, and 21 d, and it was found that the enzyme activity value in the PLGA/CaG-23.8 group was significantly higher than that in the PLGA-8 and A-7 groups. This indicates that the PLGA/CaG-23.8 scaffold is more conducive to promoting early osteoblast differentiation.

3.6.2 Qualitative and quantitative analysis of calcific nodules. Calcified nodules are indicative of osteoblast maturation, and observing these nodules is a commonly used method for studying osteoblast differentiation.[47] MC3T3-E1 cells were cultured on PLGA/CaG-23.8, A-7, and PLGA-8 for 7 d, 14 d, and 21 d, respectively. Afterward, they were stained with Alizarin

 © 2024 The Author(s). Published by the Royal Society of Chemistry

Open Access Article. Published on 15 July 2024. Downloaded on 11/10/2025 11:29:51 AM.
This article is licensed under a Creative Commons Attribution-NonCommercial 3.0 Unported Licence.

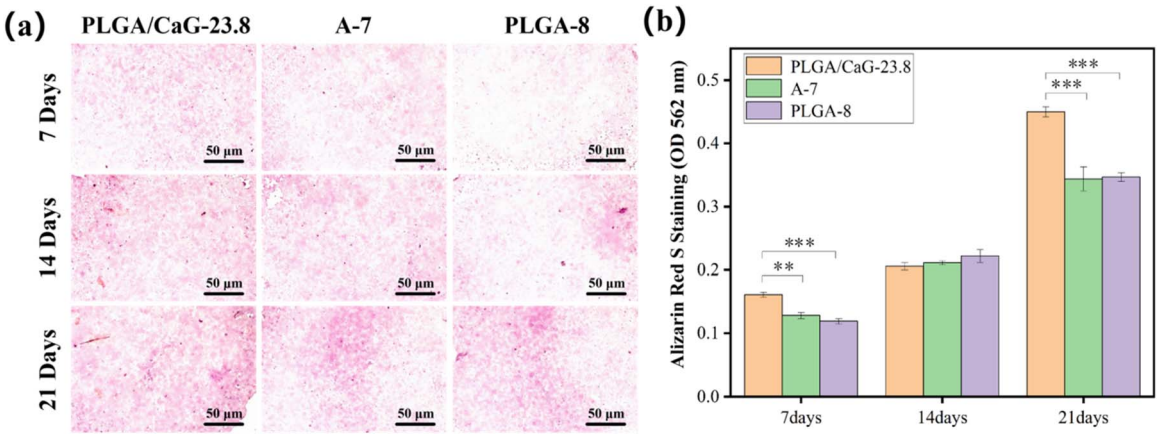

Fig. 13 Shows (a) ALP staining images and (b) quantitative analysis of ALP activity in MC3T3-E1 cells cultured on PLGA/CaG-23.8, A-7, and PLGA-8 scaffolds for 7, 14, and 21 days (**$p < 0.01$, ***$p < 0.001$).

Red S (ARS) to measure the material's absorbance at a wavelength of 562 nm. The results are presented in Fig. 13.

Fig. 13(a) displays the qualitative results of calcium nodule formation, indicating that the PLGA/CaG-23.8 group exhibits a broader range of pink calcium nodules formed at 7 d, 14 d, and 21 d. The staining becomes more pronounced as the cell culture time increases. The results indicate that the osteogenic cells in the PLGA/CaG-23.8 scaffold have a stronger mineralization ability. In comparison, there are fewer calcified nodules and lighter staining in the PLGA-8 and A-7 groups. Table 3 and Fig. 13(b) present the quantitative analysis results of calcium nodule content, which show that the calcium nodule content of the PLGA/CaG-23.8 scaffold at 7 d and 21 d is significantly higher than that of the PLGA-8 and A-7 groups. This result

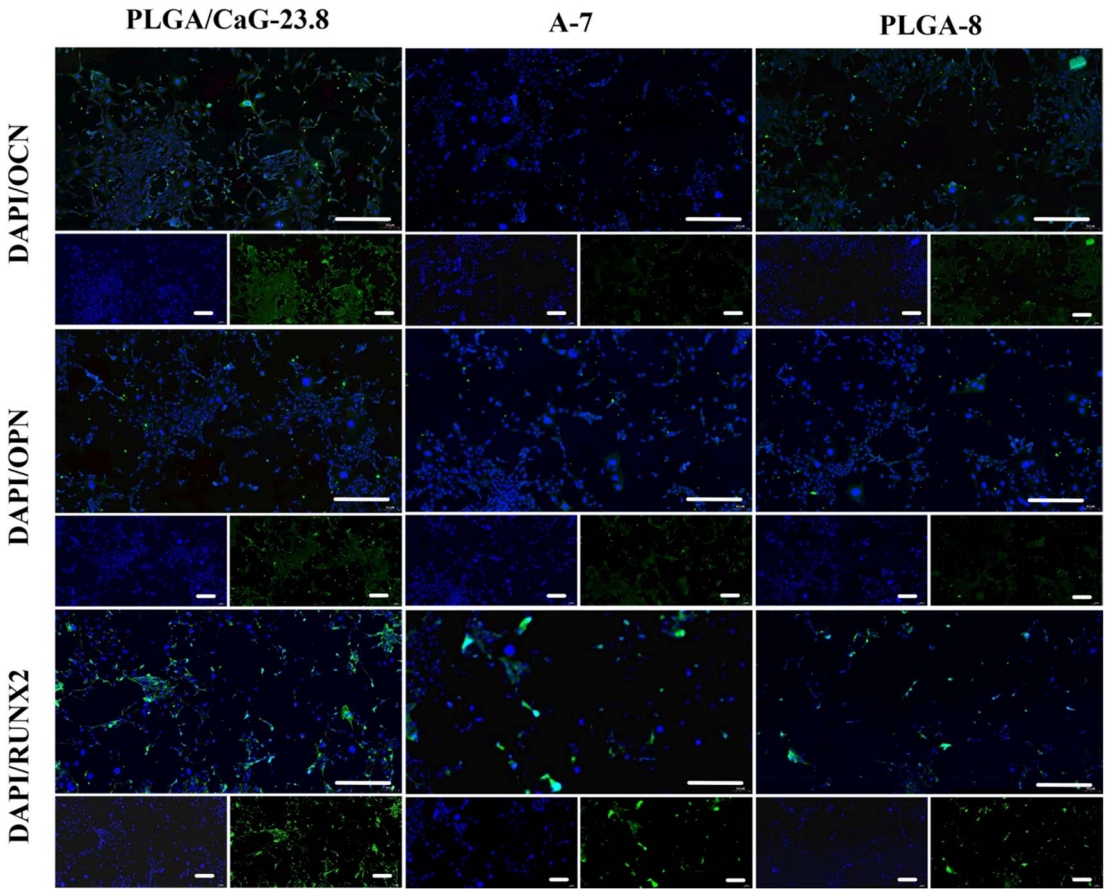

Fig. 14 Shows immunofluorescence staining images of OCN, OPN, and Runx2 in MC3T3-E1 cells cultured on PLGA/CaG-23.8, A-7, and PLGA-8 scaffolds for 7 days. Scale bar = 100 μm.

Open Access Article. Published on 15 July 2024. Downloaded on 11/10/2025 11:29:51 AM.
This article is licensed under a Creative Commons Attribution-NonCommercial 3.0 Unported Licence.

further confirms that osteogenic cells in the PLGA/CaG-23.8 scaffold have a stronger mineralization ability.

3.6.3 Osteogenic-related protein detection. Osteocalcin (OCN), osteopontin (OPN), and Runx2 are essential markers for bone cell differentiation and the formation of bone tissue.[48] This experiment demonstrates the osteogenic performance of the fiber scaffold by assessing the expression of these proteins. Fig. 14 displays immunofluorescence images of OCN, OPN, and Runx2 at 7 days after cell culture, indicating that the fluorescence intensity of OCN, OPN, and Runx2 on the PLGA/CaG-23.8 scaffold is significantly stronger compared to that on the A-7 scaffold and PLGA-8 scaffold. Only a minimal amount of OCN, OPN, and Runx2 fluorescence can be observed on the A-7 scaffold and PLGA-8 scaffold, suggesting that cells cultured on the PLGA/CaG-23.8 scaffold express a higher level of bone-related proteins. This result indicates that the PLGA/CaG-23.8 scaffold is more beneficial for promoting osteoblast differentiation and achieving *in situ* mineralization.

4 Conclusions

In this study, we successfully prepared PLGA/CaG-23.8 *in situ* mineralized bone tissue engineering scaffolds using electrospinning technology and demonstrated their *in situ* mineralization properties. The addition of CaG to the scaffolds influenced the fiber morphology, with lower concentrations of CaG resulting in finer and more uniform fibers. The optimal amount of CaG added to the scaffolds was determined to be 23.8 wt% as it exhibited the best fiber morphology. EDS energy spectrum analysis detected a high mass percentage of calcium (5.48 wt%). During the spinning process, the best fiber morphology was achieved at a voltage of 12.5 kV and a tip-to-receiver distance of 20 cm.

In vitro, simulated mineralization experiments showed that a large number of mineralized products formed on the surface of the scaffold after ALP mineralization. XRD analysis indicated that the diffraction peaks of the mineralized products were consistent with those of HAP. The results from MC3T3-E1 cell experiments showed excellent cell compatibility for the PLGA/CaG-23.8 scaffold, with a survival rate of 99.08 $\pm$ 7.05%, and well-spread cells on the scaffold. ALP activity, calcium nodule formation, and bone-related protein detection indicated that the PLGA/CaG-23.8 scaffold significantly promoted osteogenic differentiation, with MC3T3-E1 cells secreting a large amount of ALP during their growth on the scaffold, catalyzing *in situ* mineralization of CaG to form honeycomb-like structures consistent with HAP.

In summary, the PLGA/CaG-23.8 scaffolds prepared in this study have adjustable morphology, good biocompatibility, strong osteogenic differentiation ability, and the potential to play an essential role in bone defect repair, providing a feasible material for treating bone defects.

Data availability

The raw/processed data required to reproduce these findings cannot be shared as the data also form part of an ongoing study. However, detailed descriptions and summaries of the data are available within the article. Further inquiries can be directed to the corresponding author.

Author contributions

Conceptualization, L. Q. and C. T.; data curation, C. T.; formal analysis, C. T., L. Q. and S. X.; funding acquisition, S. X.; investigation, C. T., K. L., F. C. and Q. W.; methodology, L. Q. and S. X.; project administration, S. X.; resources, S. X. and L. Q.; software, C. T. and X. G.; supervision, S. X. and L. Q.; validation, S. X.; visualization, L. Q. and S. X.; writing – original draft preparation, C. T.; writing – review and editing, L. Q. and S. X. All authors have read and agreed to the published this version of the manuscript.

Conflicts of interest

The authors declare that they have no known competing financial interests or personal relationships that could have appeared to influence the work reported in this paper.

Acknowledgements

This work was supported by Chengde Biomedicine Industry Research Institute Funding project (202205B086); Research and Application of Key Technologies for Advanced Wearable Health Equipment (202305B008); Development of customized 3D printed TC4 base step channel interbody fusion device (202304B046); Research on 3D Printing of Bio-Inspired Bone Tissue and Surgical Guides (22371301D); Research and Development of 3D Printed Hydrogel-Based Skin Sensors (KY202403); Bio-3D Printed *In Situ* Mineralized Bone Tissue Engineering Scaffold (KY202406).

References

1 L. G. Karagounis and J. A. Hawley, *Int. J. Biochem. Cell Biol.*, 2010, **42**, 1376–1379.
2 D. Tang, R. S. Tare, L.-Y. Yang, D. F. Williams, K.-L. Ou and R. O. C. Oreffo, *Biomaterials*, 2016, **83**, 363–382.
3 T. Winkler, F. A. Sass, G. N. Duda and K. Schmidt-Bleek, *Bone Joint Res.*, 2018, **7**, 232–243.
4 S. Tang, Z. Dong, X. Ke, J. Luo and J. Li, *Int. J. Oral Sci.*, 2021, **13**, 42.
5 S. Jiang, X. Wang, Y. Ma, Y. Zhou, L. Liu, F. Yu, B. Fang, K. Lin, L. Xia and M. Cai, *Int. J. Nanomed.*, 2022, **17**, 783–797.
6 A. Shi, A. Heinayati, D. Bao, H. Liu, X. Ding, X. Tong, L. Wang, B. Wang and H. Qin, *Stem Cell Res. Ther.*, 2019, **10**, 1–15.
7 L. Wei, S. Wu, M. Kuss, X. Jiang, R. Sun, P. Reid, X. Qin and B. Duan, *Bioact. Mater.*, 2019, **4**, 256–260.
8 R. Dimitriou, E. Jones, D. McGonagle and P. V. Giannoudis, *BMC Med.*, 2011, **9**, 66.
9 S. S. Lee, X. Du, I. Kim and S. J. Ferguson, *Matter*, 2022, **5**, 2722–2759.

 © 2024 The Author(s). Published by the Royal Society of Chemistry

Open Access Article. Published on 15 July 2024. Downloaded on 11/10/2025 11:29:51 AM.
This article is licensed under a Creative Commons Attribution-NonCommercial 3.0 Unported Licence.

10 P. Kazimierczak, J. Kolmas and A. Przekora, *Int. J. Mol. Sci.*, 2019, **20**, 3835.
11 X. Xin, J. Wu, A. Zheng, D. Jiao, Y. Liu, L. Cao and X. Jiang, *Int. J. Nanomed.*, 2019, **14**, 1451–1467.
12 E. A. Casanova, A. Rodriguez-Palomo, L. Stähli, K. Arnke, O. Gröninger, M. Generali, Y. Neldner, S. Tiziani, A. P. Dominguez, M. Guizar-Sicairos, Z. Gao, C. Appel, L. C. Nielsen, M. Georgiadis, F. E. Weber, W. Stark, H.-C. Pape, P. Cinelli and M. Liebi, *Biomaterials*, 2023, **294**, 121989.
13 Y. Y. Qi, Z. X. Tai, D. F. Sun, J. T. Chen, H. B. Ma, X. B. Yan, B. Liu and Q. J. Xue, *J. Appl. Polym. Sci.*, 2013, **127**, 1885–1894.
14 K. Xue, X. Zhang, Z. Gao, W. Xia, L. Qi and K. Liu, *J. Transl. Med.*, 2019, **17**, 104.
15 E. A. Kamoun, S. A. Loutfy, Y. Hussein and E.-R. S. Kenawy, *Int. J. Biol. Macromol.*, 2021, **187**, 755–768.
16 Y. Sun, S. Cheng, W. Lu, Y. Wang, P. Zhang and Q. Yao, *RSC Adv.*, 2019, **9**, 25712–25729.
17 L. Parisi, A. Toffoli, G. Ghiacci and G. M. Macaluso, *J. Funct. Biomater.*, 2018, **9**, 50.
18 Y. Ning, W. Shen and F. Ao, *RSC Adv.*, 2020, **10**, 37246–37265.
19 J. Zheng, Y. Xie, T. Yoshitomi, N. Kawazoe, Y. Yang and G. Chen, *Int. J. Mol. Sci.*, 2022, **23**, 6406.
20 S. Zhang, Y. Zhao, S. Ding, C. Zhou, H. Li and L. Li, *Tissue Eng., Part A*, 2021, **27**, 1225–1238.
21 P. Liu, T. Bao, L. Sun, Z. Wang, J. Sun, W. Peng, D. Gan, G. Yin, P. Liu, W.-B. Zhang and J. Shen, *Biomater. Sci.*, 2022, **10**, 781–793.
22 Y. Liu, J. Wang, M. Jiang, X. Li, Q. Zhang and H. He, *Colloids Surf., B*, 2022, **214**, 112450.
23 G. Zheng, Z. Xie, P. Wang, J. Li, M. Li, S. Cen, S. Tang, W. Liu, G. Ye, Y. Li, S. Wang, X. Wu, H. Su, Y. Wu and H. Shen, *Cell Death Dis.*, 2019, **10**, 1–11.
24 A. Aminatun, T. Suciati, Y. W. Sari, M. Sari, K. A. Alamsyah, W. Purnamasari and Y. Yusuf, *Int. J. Polym. Mater. Polym. Biomater.*, 2023, **72**, 376–385.
25 N. Bhardwaj and S. C. Kundu, *Biotechnol. Adv.*, 2010, **28**, 325–347.
26 M. Masoudi Rad, S. Nouri Khorasani, L. Ghasemi-Mobarakeh, M. P. Prabhakaran, M. R. Foroughi, M. Kharaziha, N. Saadatkish and S. Ramakrishna, *Materials Science and Engineering: C*, 2017, **80**, 75–87.
27 G. Chen, X. Liang, P. Zhang, S. Lin, C. Cai, Z. Yu and J. Liu, *Adv. Funct. Mater.*, 2022, **32**, 2113262.
28 ISO I 10993–5:2009, *Biological evaluation of medical devices—part 5: tests for in vitro cytotoxicity*, International Organization for Standardization, Geneva, 2009, p. 34.
29 D. Wang, L. Xuan, H. Zhong, Y. Gong, X. Shi, F. Ye, Y. Li and Q. Jiang, *RSC Adv.*, 2017, **7**, 23982–23993.
30 D. Dhamecha, D. Le, R. Movsas, A. Gonsalves and J. U. Menon, *Front. Bioeng. Biotechnol.*, 2020, **8**, 799.
31 Y. Chen, J. Wang, X. Zhu, X. Chen, X. Yang, K. Zhang, Y. Fan and X. Zhang, *Regener. Biomater.*, 2018, **5**, 129–139.
32 A. Ivanoska-Dacikj, P. Makreski and G. Bogoeva-Gaceva, *J. Ind. Text.*, 2022, **51**, 4041S–4065S.
33 J. C. Ge, G. Wu, S. K. Yoon, M. S. Kim and N. J. Choi, *Nanomaterials*, 2021, **11**, 2514.
34 A. Rakhmanova, S. Kalybekkyzy, B. Soltabayev, A. Bissenbay, N. Kassenova, Z. Bakenov and A. Mentbayeva, *Nanomaterials*, 2022, **12**, 1733.
35 A. Haider, S. Haider and I.-K. Kang, *Arabian J. Chem.*, 2018, **11**, 1165–1188.
36 S. Jin, J. Yu, Y. Zheng, W.-Y. Wang, B. Xin and C.-W. Kan, *Nanomaterials*, 2018, **8**, 821.
37 D. J. Patty, A. D. Nugraheni, I. D. Ana, A. Aminatun, Y. W. Sari, G. Gunawarman and Y. Yusuf, *RSC Adv.*, 2023, **13**, 34427–34438.
38 Y. He, Y. Jin, X. Ying, Q. Wu, S. Yao, Y. Li, H. Liu, G. Ma and X. Wang, *Regener. Biomater.*, 2020, **7**, 515–525.
39 J. He, C. Chen, L. Chen, R. Cheng, J. Sun, X. Liu, L. Wang, C. Zhu, S. Hu, Y. Xue, J. Lu, H. Yang, W. Cui and Q. Shi, *Research*, 2022, **2022**, 9809763.
40 A. Patel, S. H. Zaky, K. Schoedel, H. Li, V. Sant, E. Beniash, C. Sfeir, D. B. Stolz and S. Sant, *Acta Biomater.*, 2020, **112**, 262–273.
41 W. Nie, Y. Gao, D. J. McCoul, G. J. Gillispie, Y. Zhang, L. Liang and C. He, *Int. J. Nanomed.*, 2019, **14**, 3929–3941.
42 J.-P. Chen and Y.-S. Chang, *Colloids Surf., B*, 2011, **86**, 169–175.
43 B. Nasiri-Tabrizi, W. J. Basirun, C. H. Yeong and W. M. Thein, *Ceram. Int.*, 2023, **49**, 7142–7179.
44 K. Pietryga, K. Reczyńska-Kolman, J. E. Reseland, H. Haugen, V. Larreta-Garde and E. Pamuła, *Biocybern. Biomed. Eng.*, 2023, **43**, 189–205.
45 X. Ding, X. Li, C. Li, M. Qi, Z. Zhang, X. Sun, L. Wang and Y. Zhou, *ACS Biomater. Sci. Eng.*, 2019, **5**, 4574–4586.
46 F. Zou, J. Jiang, F. Lv, X. Xia and X. Ma, *J. Nanobiotechnol.*, 2020, **18**, 1–14.
47 Y. Ma, Y. You, L. Cao, B. Liang, B. Tian, J. Dong and H. Lin, *Front. Bioeng. Biotechnol.*, 2021, **9**, 706423.
48 J. Zhu, S. Yang, K. Cai, S. Wang, Z. Qiu, J. Huang, G. Jiang, X. Wang and X. Fang, *Theranostics*, 2020, **10**, 6544–6560.